Research Square

Preprints are preliminary reports that have not undergone peer review.
They should not be considered conclusive, used to inform clinical practice,
or referenced by the media as validated information.

Electrode potential governs oxygen–oxygen bond formation through coupled interfacial dynamics

Swastika Banerjee

sbanerjee@cy.iitr.ac.in

IIT Roorkee

Ritika Saroha

Indian Institute of Technology, Roorkee, Uttarakhand

Article

Keywords: Direct O-O coupling, Constant-potential simulations, Nonadiabatic coupling, Interfacial water dynamics, Charge redistribution, Oxygen evolution reaction

Posted Date: November 27th, 2026

DOI: https://doi.org/10.21203/rs.3.rs-11875237/v1

License: This work is licensed under a Creative Commons Attribution 4.0 International License.
Read Full License

Additional Declarations: There is **NO** Competing Interest.

Electrode potential governs oxygen–oxygen bond formation through coupled interfacial dynamics

Ritika Saroha and Swastika Banerjee*

Department of Chemistry, Indian Institute of Technology Roorkee, 247667, Uttarakhand, India

E-mail: sbanerjee@cy.iitr.ac.in

Abstract

Understanding how electrode potential regulates bond formation and cleavage is central to diverse technological processes, ranging from energy storage and conversion to electrosynthesis, corrosion and electrochemical materials processing. Yet whether and how electrode potential, conventionally regarded as a thermodynamic driving force, governs the microscopic mechanisms and kinetics of these transformations remains poorly understood. Here, we address this fundamental question through the direct coupling of adjacent surface oxo species, an alternative pathway for oxygen evolution during water splitting. We combine first-principles molecular dynamics, enhanced-sampling simulations and nonadiabatic coupling analysis to investigate O–O bond formation at a hydrated Nb_2Se_2C interface. We demonstrate that constant-potential conditions facilitate the formation of adjacent oxo species and drastically reduce the O–O coupling barrier from 3.43 to 0.49 eV relative to constant-charge conditions. This pronounced change is accompanied by interfacial water reorganization, enhanced electron–nuclear coupling and nonlocal charge redistribution extending beyond the immediate reaction centre. These results highlight the importance of electrode charge regulation

and coupled interfacial dynamics in understanding chemical bond formation under electrochemical conditions. Thus, our work is the demonstration that electrode potential is not merely an external thermodynamic driving force but an essential electrochemical boundary condition that governs the pathway of catalytic bond formation.

Keywords: Direct O-O coupling, Constant-potential simulations, Nonadiabatic coupling, Interfacial water dynamics, Charge redistribution, Oxygen evolution reaction

Introduction

Electrochemical water splitting offers a route to sustainable hydrogen production by converting renewable electricity into chemical fuels.[1,2] Its efficiency, however, remains constrained by the oxygen evolution reaction (OER), a multistep process involving four-electron oxidation, proton transfer and O–O bond formation.[3,4] The complex reaction landscape, together with the electronic and spin-state requirements of oxygen formation, imposes substantial kinetic barriers and limits energy-conversion efficiency.[5–7] Understanding how O–O bonds form at electrified interfaces is therefore essential not only for improving water-oxidation catalysts but also for establishing the fundamental principles governing electrochemical bond formation.[8,9]

OER is conventionally described through the adsorbate evolution mechanism (AEM), involving sequential formation of *OH, *O and *OOH intermediates. However, the approximate linear scaling between *OH and *OOH adsorption free energies constrains their independent optimization, imposing an intrinsic limitation on catalytic activity.[10–14] Alternative mechanisms have consequently attracted considerable attention. The lattice oxygen mechanism (LOM) can circumvent conventional adsorbate scaling by incorporating lattice oxygen into molecular oxygen formation, although the associated oxygen-vacancy generation and structural reconstruction can compromise catalyst stability.[15–19] In contrast, the oxide-pathway mechanism (OPM) enables direct coupling between adjacent surface-bound oxo species, bypassing the energetically demanding *OOH intermediate without necessarily

involving lattice oxygen removal.[20,21] Its feasibility depends critically on the spatial arrangement and electronic environment of neighbouring active sites, which together determine the accessibility of O–O bond formation.[22–24] For example, Ru incorporation into MnO_2 has been shown to decrease the separation between neighbouring metal centers and facilitate direct oxygen coupling.[25] These findings establish the importance of local geometric and electronic descriptors, but leave unresolved how the surrounding electrochemical environment influences the coupling process.

Unlike bond formation in isolated molecular systems, electrochemical O–O coupling occurs at an electrified solid–liquid interface, where the electronic state of the electrode continuously interacts with the surrounding electrolyte. The applied potential, interfacial solvation and hydrogen-bond network can influence adsorbate stabilization, proton transfer and reaction energetics.[26–31] Yet these contributions are frequently examined separately, obscuring how electronic redistribution and molecular reorganization evolve together during bond formation. Conventional density functional theory approaches based on the computational hydrogen electrode provide valuable thermodynamic descriptors but typically evaluate reaction intermediates within fixed-electron-number calculations.[32,33] Although potential-dependent free-energy corrections can be introduced, such treatments do not explicitly capture the continuous adjustment of electrode charge during a reaction or its coupling to solvent dynamics.[34–36] Grand-canonical constant-potential methods address this limitation by allowing electron exchange with a reservoir while maintaining a prescribed electronic chemical potential.[37–39] This distinction is particularly important for reactions involving substantial charge redistribution and simultaneous bond formation and cleavage. Whether potential-dependent electronic relaxation also modifies electron–nuclear coupling and the spatial extent of charge redistribution during O–O bond formation remains an important mechanistic question.

Transition-metal carbochalcogenides provide a promising platform for investigating these effects.[40,41] Combining carbide-based frameworks with chalcogen-containing coordination environments, these layered materials bridge structural features of MXenes and transition-

metal dichalcogenides (TMDCs), two material families extensively explored for electrocatalytic applications.[42–44] Whereas many TMDCs undergo anodic surface reconstruction to form catalytically active metal (oxy)hydroxides, the catalytic behaviour of MXenes is strongly influenced by their surface terminations.[45–47] Transition-metal carbochalcogenides, first exemplified by Ta_2S_2C, offer an alternative combination of metal–carbon and metal–chalcogen bonding environments.[48] Related layered compounds, including Ta_2Se_2C and Nb_2S_2C, have attracted interest for their electronic and energy-related properties.[41,49] Notably, Nb_2Se_2C exhibits promising OER activity, delivering 10 $mA\,cm^{-2}$ at an overpotential of 321 mV.[50] However, the elementary reaction pathways underlying this activity, particularly how the electrified electrode–electrolyte interface influences O–O bond formation and reaction kinetics, remain poorly understood.

Here we investigate how electrode potential regulates direct O–O bond formation at the hydrated Nb_2Se_2C interface using a constant-potential hybrid solvation–dynamics framework that combines explicit interfacial water with implicit solvation and grand-canonical electronic equilibration.[51,52] By integrating first-principles molecular dynamics, constrained reaction-coordinate sampling and nonadiabatic coupling analysis,[53] we resolve the evolution of surface oxidation, O–O bond rearrangement and the accompanying interfacial response under constant-charge and constant-potential conditions. We show that electrode charge regulation promotes the formation of adjacent oxo species and substantially lowers the barrier for their direct coupling. This potential dependence is accompanied by solvent reorganization, enhanced electron–nuclear coupling and nonlocal electronic charge redistribution extending into the surrounding electrode framework. These findings establish a molecular-level connection between electrochemical boundary conditions and collective interfacial dynamics, providing a broader perspective on how electrode potential governs chemical bond formation.

Results and discussion

Structural characteristics and interfacial water organization

The structural and interfacial characteristics of Nb_2Se_2C/water were examined to establish the molecular environment governing electrochemical oxygen evolution. As shown in Fig.1a, Nb_2Se_2C adopts a layered structure with an interlayer separation of 3.04 Å. Each layer comprises interconnected C@Nb_6 and Nb@C_3Se_3 octahedral units, with C coordinated by six Nb atoms and Nb surrounded by three C and three Se atoms (Fig.1a). The optimized unit-cell volume deviates from the experimental value by only 1.74% (Supplementary Fig. S1), supporting the reliability of the structural model. To describe the electrode–electrolyte interface, a $(1\bar{1}0)$ Nb_2Se_2C slab was interfaced with a 10.5 Å-thick explicit water region, supplemented by 12Å of implicit solvation (Fig. 1b). The interface was equilibrated through 10 ps of constant-charge *Ab initio* molecular dynamics (AIMD), followed by 5 ps of AIMD incorporating implicit solvation. Subsequent constant-charge (CCM) and constant-potential (CPM) simulations were employed to distinguish the effects of fixed electron number from those of electrode charge regulation. In CPM, the electronic chemical potential is maintained at a prescribed target through iterative adjustment of the electron population, allowing the electrode to respond electronically to changes in the interfacial configuration.

The time-averaged water-density profile reveals pronounced molecular organization at the Nb_2Se_2C/water interface (Fig. 1c). A prominent density maximum of approximately 2.4 $\mathrm{g\,cm^{-3}}$ occurs at $c \approx 13.5$–14Å, corresponding to approximately 1.5–2.0Å from the nominal surface boundary at $c \approx$12Å. This density substantially exceeds the bulk-water reference (1.0 $\mathrm{g\,cm^{-3}}$), indicating preferential water accumulation adjacent to the catalyst surface, consistent with its hydrophilic character. The position of this maximum remains largely insensitive to the spatial averaging window (Supplementary Fig. S2), supporting the robustness of the first hydration layer. Additional density oscillations extend across the explicit solvent region, indicating that surface-induced water organization persists beyond the imme-

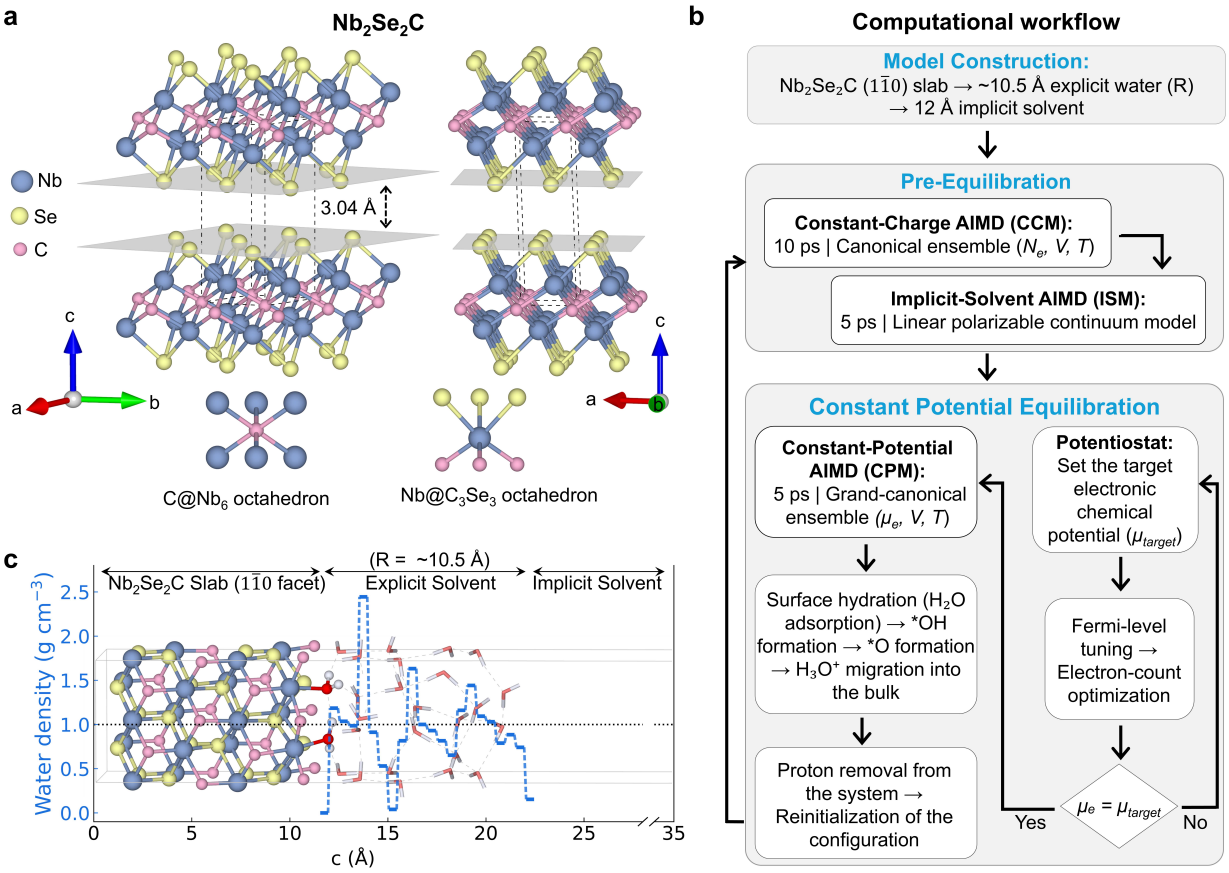

Figure 1: **Crystal structure, computational workflow and interfacial water organization.** **a,** Optimized crystal structure of Nb_2Se_2C, showing the layered arrangement, interlayer separation of 3.04 Å, and local C and Nb octahedral coordination environments. **b,** Computational workflow for constant-charge (CCM) and constant-potential (CPM) ab initio molecular dynamics simulations of the Nb_2Se_2C/water interface, including structural equilibration, surface oxidation and iterative adjustment of the electronic chemical potential. **c,** Time-averaged water-density profile along the surface-normal direction (c) of the (1$\bar{1}$0) Nb_2Se_2C/water interface, obtained from 5 ps of constant-charge AIMD with explicit interfacial water and implicit solvation, following 10 ps of pre-equilibration. The density was evaluated using a 0.5 Å spatial averaging window. The horizontal dashed line indicates the bulk-water density ($1.0\,\mathrm{g\,cm^{-3}}$).

diate hydration layer without reaching a sustained bulk-like distribution within the sampled region. These results establish a heterogeneous electrode–electrolyte interface in which the $(1\bar{1}0)$ Nb_2Se_2C catalyst surface and structured interfacial water provide the setting for surface oxidation and proton transfer. The explicit treatment of electrode charge regulation (detailed in Fig. 1b) further enables the influence of electrochemical boundary conditions on interfacial restructuring and subsequent O–O coupling to be examined.

Potential-dependent surface oxidation and interfacial proton transport

The pronounced organization of interfacial water (Fig. 1c) raises the question of how this hydrogen-bonded environment responds to changes in electrode potential and participates in surface oxidation. To investigate this, we monitored the evolution of two adjacent Nb-bound water molecules through successive AIMD simulations under CCM, implicit-solvent (ISM), and CPM conditions (Fig. 2). The simulations were initiated from a doubly hydrated surface, denoted as $*H_2O*H_2O$, and followed its sequential conversion into the neighboring oxo configuration, *O*O, through two successive oxidation stages.

During the initial 15 ps of CCM and ISM equilibration, both adsorbed water molecules remain intact, with no persistent hydroxyl or oxo species detected (Fig. 2a, left). The corresponding spatial distributions show predominantly molecular water extending approximately 1–11Å from the Nb active sites, without any hydronium formation (Fig. 2b, c, left). A distinct change occurs upon switching to CPM at 15 ps. The initially hydrated surface undergoes rapid deprotonation, passing through transient $*H_2O*OH$ and *OH*OH configurations before predominantly forming $*H_2O*O$ within approximately 1 ps. Although brief returns to partially hydroxylated (*OH*OH) configurations occur, the oxidized state ($*H_2O*O$) remains dominant during the subsequent trajectory. The onset of deprotonation upon imposing constant potential, following its absence during the preceding equilibration stages, indicates that electrode charge regulation strongly influences the accessibility of sur-

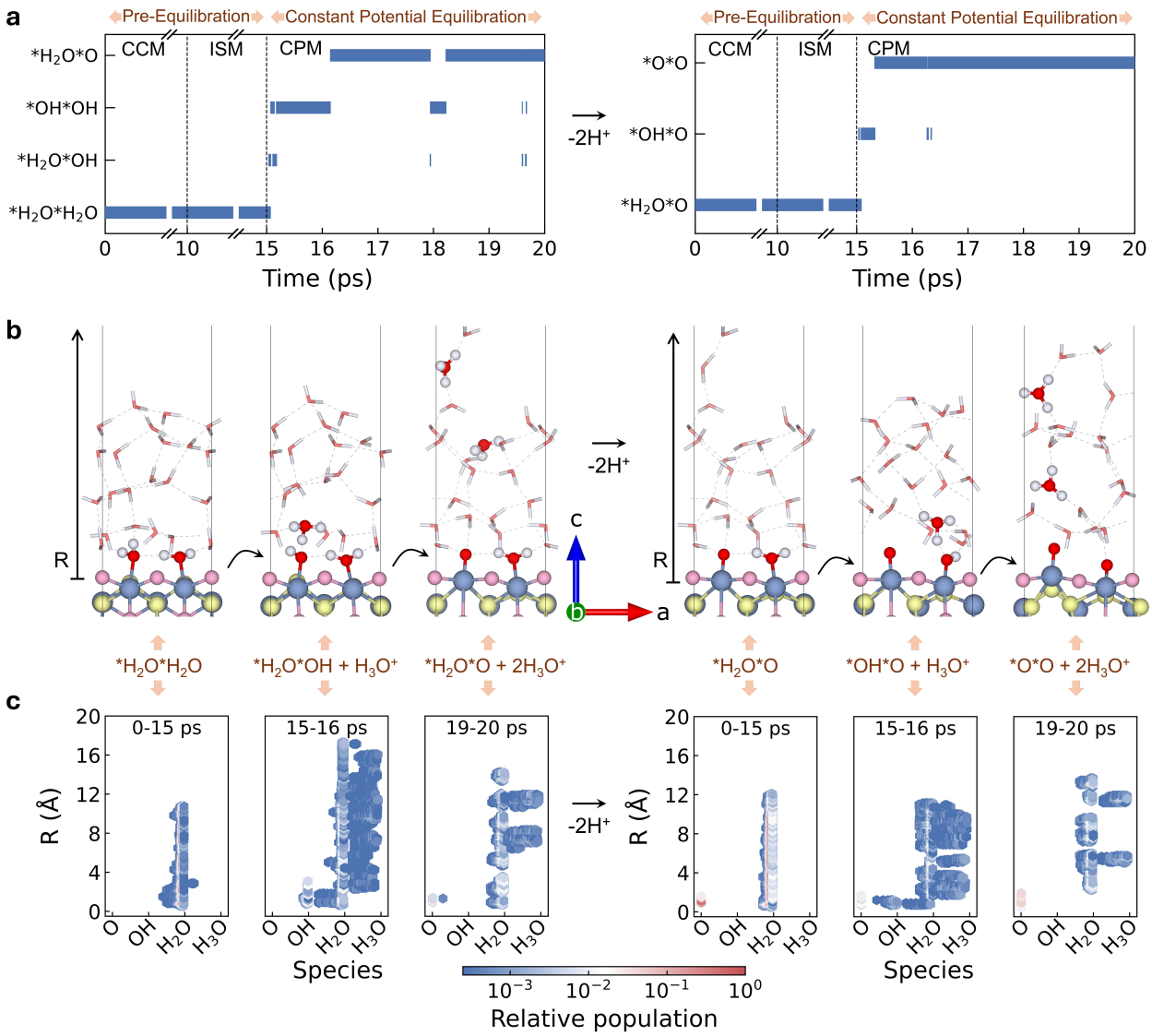

Figure 2: **Potential-dependent surface oxidation and proton redistribution at the Nb_2Se_2C/water interface. a,** Time evolution of surface-bound species during the sequential oxidation of adjacent Nb-bound water molecules, from $*H_2O*H_2O$ to $*H_2O*O$ (left) and subsequently to *O*O (right). Each 20 ps AIMD trajectory comprises constant-charge equilibration (CCM, 0–10 ps), implicit-solvent equilibration (ISM, 10–15 ps), and constant-potential dynamics (CPM, 15–20 ps). Blue segments indicate the residence intervals of the corresponding surface configurations. **b,** Representative AIMD snapshots showing successive deprotonation of the adsorbed water molecules and proton transfer into the surrounding water network, forming H_3O^+. Following the first oxidation stage, two excess protons are removed before initiating the second stage. The surface-normal direction is along c, and R denotes the distance from the Nb active sites. **c,** Spatial distributions of O, OH, H_2O, and H_3O^+ as a function of distance R during the initial (0–15 ps), early constant-potential (15–16 ps), and final (19–20 ps) intervals of the two oxidation stages. Marker colours represent the relative populations of the identified species. The asterisk (*) denotes adsorption at a surface Nb site.

face oxidation under the simulated conditions.

The oxidation of surface-bound water is accompanied by proton redistribution into the surrounding hydrogen-bonded network (Fig. 2b, c, left). The released protons are accommodated by neighboring water molecules as H_3O^+, rather than remaining associated with the Nb adsorption sites. During the initial CPM interval (15–16 ps), hydronium species appear at distances extending to approximately 17Å from the active sites, indicating that proton transfer can extend well beyond the immediate surface coordination environment (Fig. 2c, left). By 19–20 ps, the surface is predominantly occupied by $*H_2O*O$, while the hydronium population is concentrated within distinct regions at approximately 6–12Å. This evolution suggests that surface deprotonation and subsequent proton accommodation are spatially separated processes, with the surrounding water network providing the medium for redistribution of the released protons.

To examine further oxidation, the two excess protons generated during the first stage were removed, and a second AIMD sequence was initiated from the $*H_2O*O$ configuration (Fig. 2a, right). As observed previously, the surface remains chemically stable throughout the initial CCM and ISM equilibration. Upon switching to CPM, the remaining adsorbed water molecule undergoes rapid deprotonation through a short-lived *OH*O intermediate, yielding the doubly oxidized *O*O configuration within approximately 0.5 ps. This configuration persists throughout most of the remaining trajectory, apart from brief proton back-transfer events. The corresponding snapshots reveal the formation of additional H_3O^+ species as the second adsorbed water molecule loses its protons (Fig. 2b, right).

The spatial distributions further distinguish the proton-transfer environments of the two oxidation stages (Fig. 2c). During the early CPM interval of the second stage, surface-bound O and transient OH species coexist near the Nb sites, while hydronium populations extend approximately 3–11Å into the solvent. By 19–20 ps, the surface is predominantly occupied by adjacent oxo species, with H_3O^+ distributed mainly between approximately 5 and 13Å. Compared with the first oxidation stage, the generated hydronium species remain relatively

closer to the surface during the second stage. These differences suggest that proton redistribution is sensitive to the evolving oxidation state of the catalyst and the associated interfacial hydration environment. Nevertheless, the spatial distributions represent the sampled proton populations and do not independently resolve individual proton-transfer pathways or their kinetics.

Overall, the two successive AIMD trajectories establish a potential-dependent pathway for converting neighboring adsorbed water molecules into surface-bound oxo species,

$$*H_2O*H_2O \longrightarrow *H_2O*O \longrightarrow *O*O, \tag{1}$$

with each oxidation stage accompanied by the release of two protons into the surrounding aqueous environment. The absence of sustained deprotonation during the preceding CCM and ISM intervals, followed by rapid oxidation under CPM, highlights the importance of allowing the electrode electron population to respond to the evolving interfacial configuration. Importantly, the released protons are accommodated within the solvent rather than remaining bound to the reactive Nb sites, indicating that surface oxidation and proton redistribution are coupled through the interfacial water network. The formation and persistence of adjacent *O species provide the essential surface configuration for direct O–O coupling through OPM. Thus, constant-potential conditions not only influence the electronic response of the catalyst but also facilitate the generation of the reactive oxo intermediates from which O–O bond formation can proceed. Whether these neighboring oxygen species subsequently couple, and how the electrochemical boundary condition influences the associated reaction barrier, requires examination of the O–O bond-formation pathway.

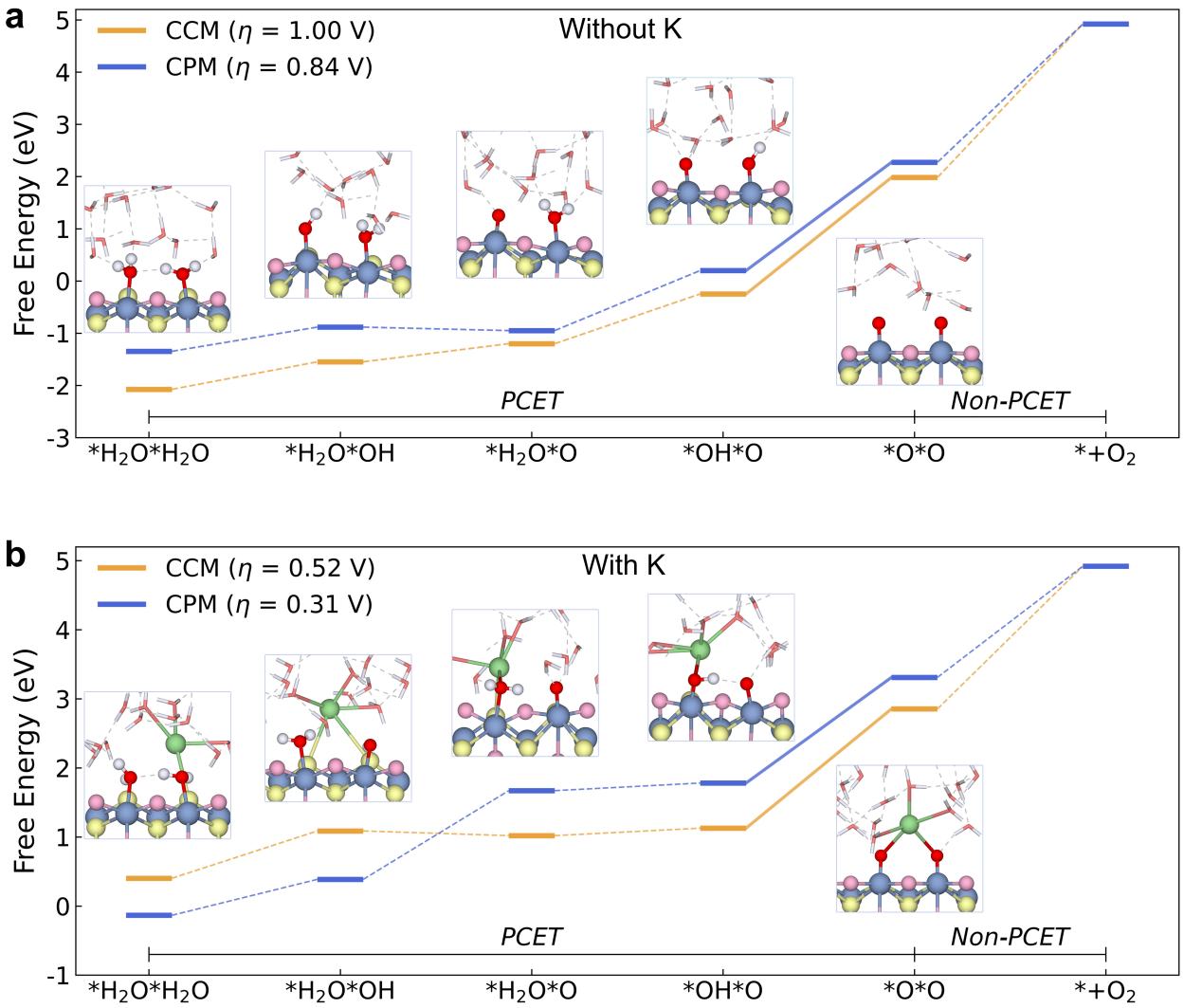

Figure 3: **Potential- and cation-dependent thermodynamics of oxygen evolution on Nb_2Se_2C.** Free-energy profiles for oxygen evolution through the oxide-pathway mechanism under constant-charge (CCM, orange) and constant-potential (CPM, blue) conditions **a,** without and **b,** with interfacial K^+. The reaction comprises four proton-coupled electron-transfer (PCET) steps leading to adjacent surface-bound oxo species (*O*O), followed by non-PCET O–O coupling and oxygen release. The corresponding overpotentials (η) are indicated. Insets show representative optimized intermediate configurations under CPM.

Potential- and cation-dependent thermodynamics of oxygen evolution

The spontaneous formation of adjacent surface-bound oxo species under constant-potential conditions (Fig. 2) identifies a possible precursor for direct O–O coupling. To assess the ther-

modynamic feasibility of this pathway, we evaluated the OER through the OPM, as the conventional AEM pathway is energetically disfavoured by the substantial free-energy penalty associated with *OOH formation (Supplementary Fig. S3). The OPM proceeds through four successive proton-coupled electron-transfer (PCET) steps, converting $*H_2O*H_2O$ into *O*O, followed by non-PCET O–O coupling and oxygen release (Fig. 3).

In the absence of K^+, the first three PCET steps are comparatively less demanding, whereas the final oxidation of *OH*O to *O*O presents the largest free-energy increase and determines the limiting potential (Fig. 3a). The corresponding overpotential decreases from 1.00 V under CCM to 0.84 V under CPM, indicating that electrode charge regulation improves the thermodynamic accessibility of the doubly oxidized surface. This finding is consistent with the rapid formation of adjacent oxo species observed during constant-potential AIMD.

The presence of interfacial K^+ further alters the reaction energetics (Fig. 3b). Although the final PCET step remains potential-determining under both electrochemical descriptions, the overpotential decreases from 0.52 V under CCM to 0.31 V under CPM, with the latter in close agreement with experimental measurements of 321 mV.**??** Thus, combining constant-potential conditions with K^+ incorporation reduces the predicted overpotential by 0.69 V relative to the pristine surface under CCM. The optimized configurations reveal that K^+ interacts with the oxygen-containing adsorbates and surrounding water molecules, suggesting that local electrostatic interactions and solvation contribute to the stabilization of reaction intermediates. These results establish that both electrode charge regulation and interfacial cations substantially influence the thermodynamics of surface oxidation, facilitating the formation of adjacent oxo species required for the OPM. However, the thermodynamic accessibility of *O*O does not establish the kinetic feasibility of subsequent O–O bond formation. The subsequent section examines the O–O bond-rearrangement pathway and its activation barrier under constant-charge and constant-potential conditions.

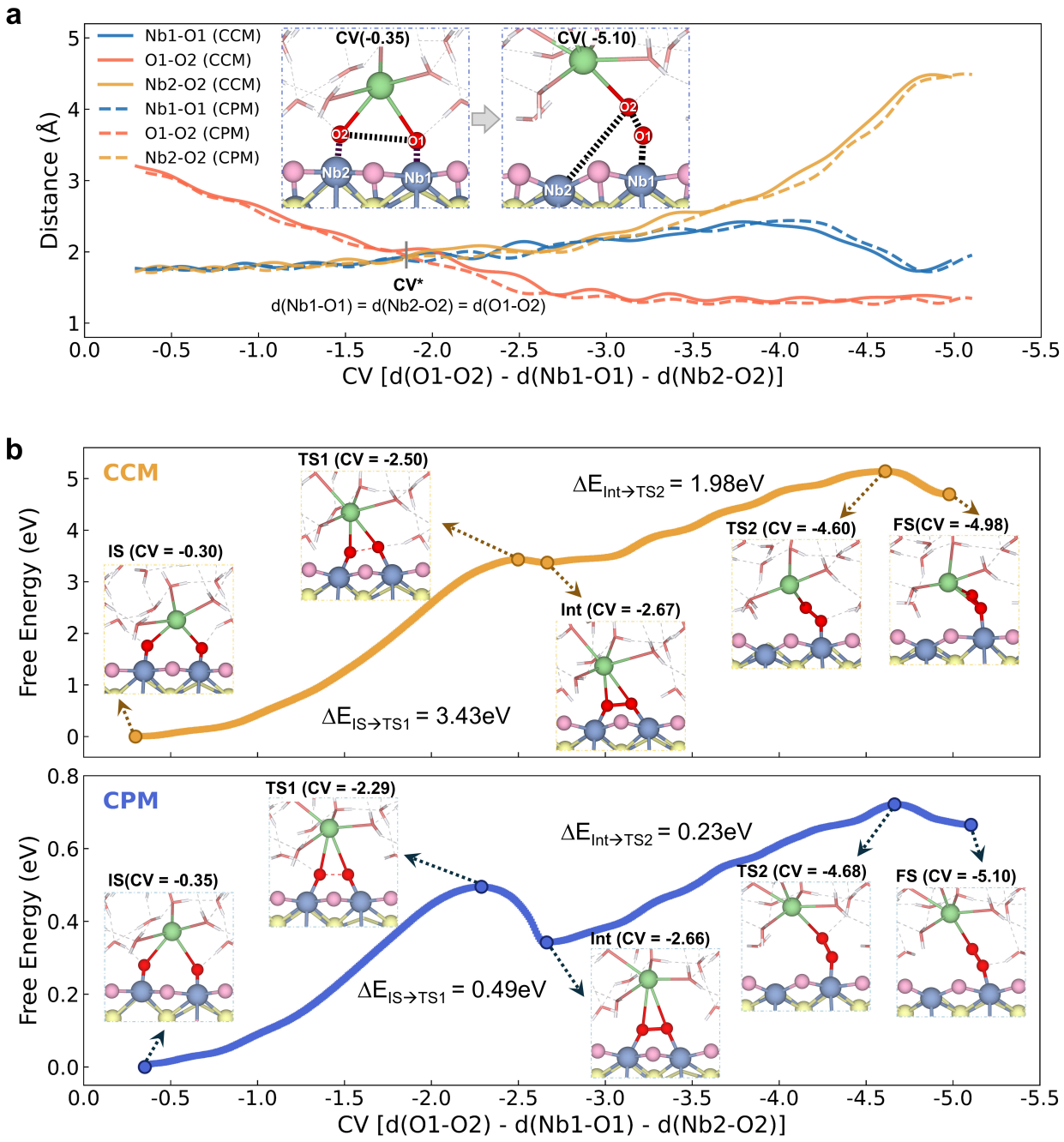

Figure 4: **Enhanced-Sampling simulation of O-O Coupling in Oxide-Path Oxygen Evolution Reaction: a,** Variation of the key interatomic distances governing the coupling event, d(O1-O2), d(Nb1-O1), and d(Nb2-O2), along the reaction coordinate sampled by slow-growth ab initio molecular dynamics. The collective variable (CV) is defined as d(O1-O2) - d(Nb1-O1) - d(Nb2-O2) and CV* denotes the point at which d(O1-O2) = d(Nb1-O1) = d(Nb2-O2). Free-energy profiles of the O-O coupling step as a function of the CV, obtained by slow-growth sampling under two electrochemical boundary conditions: **b, upper panel** constant-charge (CCM) and **b, lower panel** constant-potential (CPM).

Potential-dependent reaction pathway and kinetics of direct O–O coupling

To shed light on the kinetic feasibility of the subsequent O–O bond formation, we investigated the direct coupling of two surface-bound oxo species using slow-growth AIMD under CCM and CPM conditions (Fig. 4). The reaction was described by a collective variable (CV) incorporating the O–O separation and the two Nb–O coordination distances,

$$\mathrm{CV} = d_{\mathrm{O1-O2}} - d_{\mathrm{Nb1-O1}} - d_{\mathrm{Nb2-O2}}. \tag{2}$$

This collective coordinate (CV) simultaneously captures the approach of the two reactive oxygen species and their progressive detachment from the surface Nb centers. As O–O association proceeds, the decreasing O1–O2 separation and subsequent elongation of the Nb–O bonds drive the CV toward increasingly negative values. Importantly, CV does not prescribe the sequence of bond formation and dissociation, allowing their relative progression to emerge from the molecular dynamics. The system was driven along this coordinate at a constant rate, and the corresponding work accumulated during the slow-growth trajectories was used to construct the reaction free-energy profiles.

The structural evolution along the CV reveals a two-stage coupling mechanism, comprising O–O bond formation followed by asymmetric Nb–O bond cleavage (Fig. 4a). During the initial stage (CV ≈ 0 to -2.65), the O1–O2 distance contracts substantially from approximately 3.11 to 1.42Å, approaching the characteristic bond length of a superoxo-like O–O species. Notably, both Nb1–O1 and Nb2–O2 distances remain nearly unchanged at approximately 1.8–2.1Å throughout this interval. Thus, the two oxygen species approach and establish an O–O bond while remaining coordinated to their respective surface Nb centers, producing a doubly anchored Nb1–O1–O2–Nb2 bridging intermediate. Along this pathway, the system passes through a characteristic configuration near CV ≈ -1.85, where the O1–O2, Nb1–O1, and Nb2–O2 distances become comparable (denoted as CV* in Fig. 4a). This con-

figuration marks an intermediate stage of structural reorganization preceding the formation of the fully developed O–O bridge.

Beyond CV ≈ -2.75, the reaction proceeds through a distinctly asymmetric rearrangement of the metal–oxygen coordination environment. While the Nb1–O1 distance remains close to 2.1Å, the Nb2–O2 distance increases progressively to approximately 4.5Å, indicating dissociation of the latter bond. The persistence of the Nb1–O1 interaction, together with the detachment of O2 from Nb2, converts the doubly anchored bridging intermediate into an end-on O–O species coordinated to a single surface Nb center. The initial and final configurations, corresponding to CV $= -0.35$ and -5.01 for CPM, respectively, are illustrated in the insets of Fig. 4a. These structural changes establish that direct O–O coupling does not require the simultaneous cleavage of both Nb–O bonds. Instead, O–O association occurs while both oxygen species remain surface-bound, followed by selective dissociation of one Nb–O bond. The corresponding free-energy profiles (Fig. 4b) reproduce this sequential structural transformation, with the initial state (IS) evolving through a first transition state (TS1) into the bridging Nb1–O1–O2–Nb2 intermediate (Int), followed by a second transition state (TS2) associated with Nb2–O2 bond dissociation and the formation of the final state (FS). Despite the common structural sequence, the reaction energetics exhibit a striking dependence on the electrochemical boundary conditions. Under CCM (Fig. 4b, upper panel), the first O–O coupling step encounters a substantial free-energy barrier of 3.43 eV, rendering the direct coupling pathway strongly kinetically hindered. In contrast, CPM reduces this barrier to only 0.49 eV (Fig. 4b, lower panel), corresponding to a sharp decrease of approximately 86%, relative to CCM. This nearly sevenfold reduction in the barrier magnitude demonstrates that maintaining a constant electrode potential dramatically enhances the energetic accessibility of direct O–O bond formation. This pronounced difference further highlights that the thermodynamic feasibility inferred from the preceding PCET steps, as discussed in the previous section, does not necessarily translate into kinetic accessibility of O–O bond formation without an appropriate description of the electrode's electronic response.

The origin of this potential-dependent O–O coupling barriers can be understood in terms of the different electronic constraints imposed by the two electrochemical descriptions: CCM and CPM. While CCM restricts electronic redistribution to a fixed electron population, CPM allows electron exchange with an external reservoir, enabling the electrode charge to adjust to the evolving reaction geometry. This additional degree of electronic relaxation can modify local electrostatic interactions and screening, potentially stabilizing the transition-state configurations. Such charge regulation is inherently coupled to the interfacial solvent environment, as changes in electrode charge can modulate the local electric field, water orientation and hydrogen-bond (HB) connectivity. The reduced kinetic barrier under CPM may therefore arise from the interplay between electronic relaxation and solvent reorganization. To examine the solvent contribution to this coupled interfacial response, we next analyze the evolution of water-dipole orientation and HB connectivity along the reaction coordinate under CCM and CPM (Fig. 5).

Potential-dependent interfacial water reorganization during O–O coupling

Solvent reorganization during O–O coupling was characterized by tracking the evolution of interfacial water-dipole orientations and hydrogen-bond (HB) connectivity along the CV under both CCM and CPM (Fig. 5). To quantify water-dipole orientation, we introduced two projection-weighted order parameters, $\mu(A)^+$ and $\mu(A)^-$, defined with respect to the angle A between the water-dipole unit vector, $\hat{\mathbf{d}}$, and a reference direction. Two complementary reference axes were considered: the outward surface normal, $\hat{\mathbf{n}}$, defining the angle α, and the radial unit vector, $\hat{\mathbf{r}}$, directed from the midpoint of the reactive O–O species toward the oxygen atom of each surrounding water molecule, defining the angle θ (Fig. 5a). The corresponding angular projections are expressed as $\cos\alpha = \hat{\mathbf{d}} \cdot \hat{\mathbf{n}}$ and $\cos\theta = \hat{\mathbf{d}} \cdot \hat{\mathbf{r}}$. The negative-orientation contribution is defined as

$$\mu(A)^- = \frac{\sum_{\cos A_i<0} |\cos A_i|}{\sum_i |\cos A_i|}, \qquad A = \alpha, \theta, \tag{3}$$

where the complementary positive-orientation contribution satisfies $\mu(A)^+ + \mu(A)^- = 1$. The $|\cos A|$ weighting emphasizes dipoles aligned parallel or antiparallel to the reference direction while suppressing contributions from nearly perpendicular orientations. Thus, $\mu(A)^-$ measures the relative magnitude of negatively projected dipole components rather than simply the fraction of water molecules pointing in a particular direction. A value of 0.5 corresponds to equal weighted contributions from positive and negative projections, as indicated by the dashed horizontal line in Fig. 5b. For an isotropic orientational distribution, $\mu(A)^- = 0.5$; however, the same value can also arise from a nonisotropic distribution with balanced positive and negative contributions. Since the two order parameters are complementary, only $\mu(A)^-$ is presented.

The evolution of $\mu(\alpha)^-$ reveals a distinction between the two electrochemical boundary conditions (Fig. 5b, left panel). Under CCM, $\mu(\alpha)^-$ remains predominantly between 0.6 and 0.8 throughout the reaction coordinate, from the IS to the FS. This persistent deviation above 0.5 indicates that the interfacial water dipoles retain a preferential component directed toward the surface, with comparatively limited changes during the initial O–O association and subsequent Nb–O bond dissociation. In contrast, CPM produces a substantially more dynamic orientational response. Starting from approximately 0.6–0.7 near the IS, $\mu(\alpha)^-$ progressively decreases toward 0.5 between the TS1 and TS2, with several interfacial populations exhibiting values below 0.5. Beyond TS2, the negative-orientation contribution decreases further, approaching approximately 0.3 toward the FS. This evolution indicates a transition from predominantly surface-directed dipole components toward a preference for orientations opposing the initial polarization as the reaction proceeds. Importantly, this change occurs over the same reaction-coordinate interval in which the doubly anchored O–O intermediate undergoes asymmetric Nb2–O2 bond cleavage, suggesting that the evolving

surface coordination environment is accompanied by substantial solvent reorientation under CPM.

The orientation of water relative to the reactive O–O center provides an additional perspective on this response. Under CCM, $\mu(\theta)^-$ fluctuates around the equal-contribution value of 0.5 during much of the initial O–O coupling process, with more pronounced deviations emerging beyond TS2 as the system approaches the FS (Fig. 5b, right panel). This behavior suggests that the local dipolar organization around the reactive oxygen species undergoes comparatively modest net changes during the formation of the bridging intermediate, followed by a more substantial rearrangement during the final bond-dissociation stage. Under CPM, however, $\mu(\theta)^-$ remains predominantly below 0.5 over a larger portion of the reaction coordinate, particularly beyond TS1, with typical values of approximately 0.2–0.4 around the intermediate and subsequent reaction stages. The reduced negative-orientation contribution indicates a preference for water-dipole components aligned with the radial direction extending outward from the reactive O–O center. Consequently, while the surface-normal projection describes the overall interfacial polarization, the radial projection reveals a more localized reorganization of water around the evolving oxygen species. Their contrasting responses demonstrate that potential-dependent solvent restructuring cannot be represented by a single surface-normal orientational descriptor.

The spatial extent of this reorganization was further examined by varying the distance cutoff R used to select water molecules from the active surface, spanning approximately 5–10Å (Fig. 5b). The resulting curves are color-coded from blue to red with increasing R. Under CCM, the cutoff-dependent profiles of $\mu(\alpha)^-$ remain relatively close throughout much of the reaction coordinate, consistent with the persistence of a common surface-directed orientational preference across the sampled interfacial region. Under CPM, the response becomes considerably more heterogeneous. The smallest sampling regions ($R \approx$ 5–6Å) exhibit pronounced fluctuations in both $\mu(\alpha)^-$ and $\mu(\theta)^-$, particularly around the transition-state regions, whereas the profiles obtained with larger cutoffs ($R \approx$ 9–10Å) are compara-

tively smoother. At selected reaction-coordinate values, the separation between the cutoff-dependent orientational contributions reaches approximately 0.15–0.25. Since the cutoff regions are cumulative rather than independent solvation shells, these differences indicate that the inclusion of water molecules farther from the reactive surface progressively modifies the averaged orientational response. The stronger fluctuations observed for smaller R therefore suggest that the most pronounced potential-dependent reorientation is concentrated near the reactive interface, while the additional water molecules included at larger distances moderate the overall response.

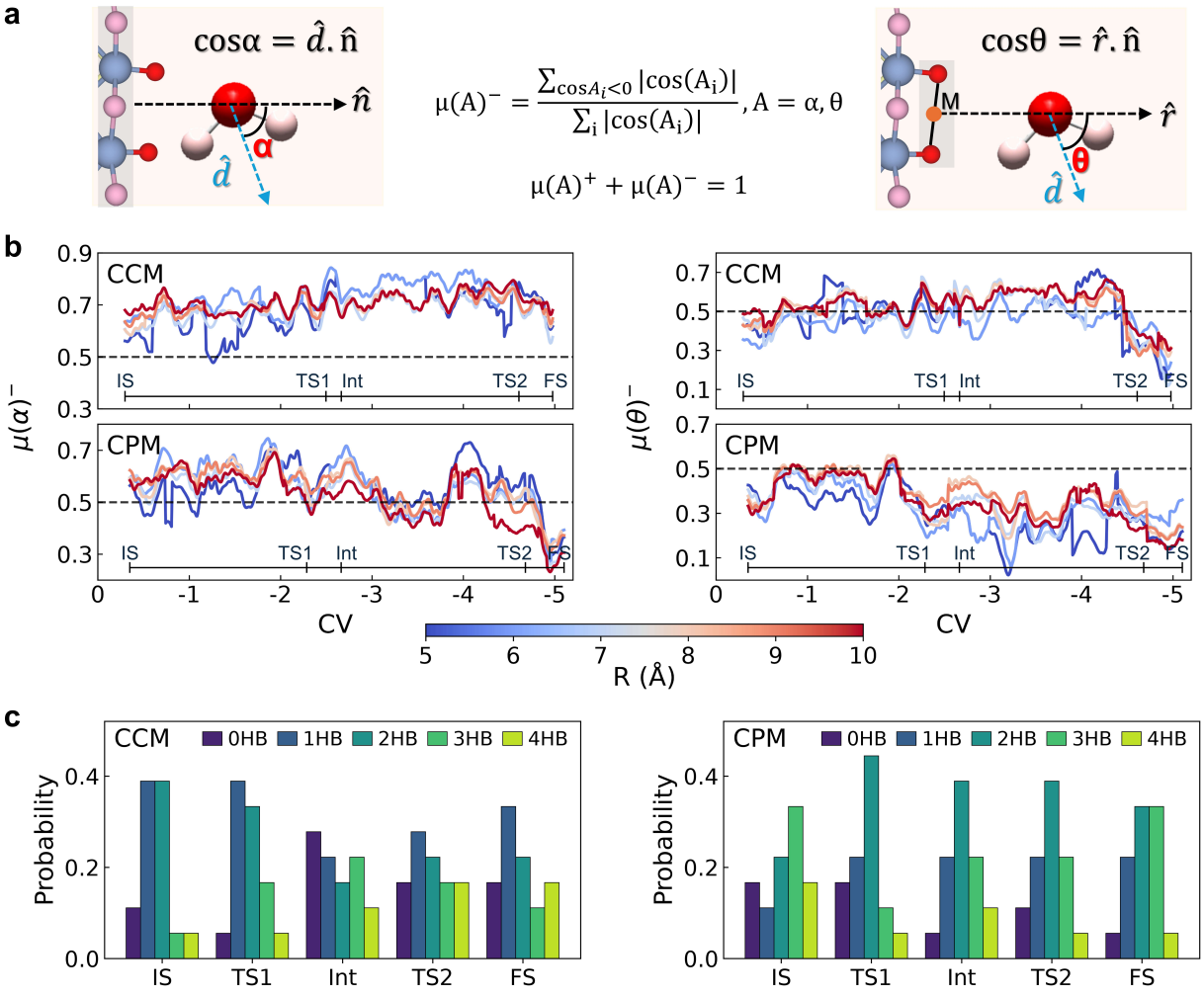

Figure 5: **Orientational response and hydrogen-bonding dynamics of interfacial water during O–O coupling. a,** Schematic representations of the water-dipole orientation relative to (i) the surface normal (α) and (ii) the vector connecting the midpoint of the reactive surface O–O species to the water oxygen (θ). The corresponding unit vectors are denoted by $\hat{\mathbf{d}}$, $\hat{\mathbf{n}}$, and $\hat{\mathbf{r}}$, respectively. Negative projections ($\cos\alpha < 0$) or ($\cos\theta < 0$) indicate dipole orientations opposing the respective reference directions. **b,** Evolution of the normalized, cosine-weighted negative-orientation contributions, (left panel) ($\mu(\alpha)^-$) and (right panel) ($\mu(\theta)^-$), along the collective variable (CV) under constant-charge (CCM) and constant-potential (CPM) conditions. Each curve represents a cumulative selection of interfacial water molecules within a cutoff distance (R) from the active surface, as indicated by the color scale. The dashed horizontal line at 0.5 denotes equal weighted contributions from positive and negative dipole projections. **c,** Probability distributions of interfacial water molecules forming 0–4 hydrogen bonds (HBs) at the initial state (IS), first transition state (TS1), intermediate (Int), second transition state (TS2), and final state (FS) under CCM (left panel) and CPM (right panel) conditions. Hydrogen bonds are identified using a distance cutoff of 1.8 Å.

To determine whether this orientational reorganization is accompanied by changes in the local hydration network, we analyzed the hydrogen-bond (HB) coordination of interfacial water at representative configurations corresponding to IS, TS1, the bridging intermediate (Int), TS2, and FS (Fig. 5c). HB between neighboring water molecules were identified using a geometric H$\cdots$O distance cutoff of 1.8Å, selected following a systematic examination of the cutoff dependence (Supplementary Figs. S4 and S5). This criterion distinguishes water molecules forming zero to four hydrogen bonds, denoted as 0HB–4HB, allowing the evolution of undercoordinated and more extensively hydrogen-bonded environments to be compared along the reaction pathway.

Under CPM, the IS is dominated by 3HB configurations ($\sim$33%), with 4HB, 2HB and 0HB each contributing $\sim$20% (Fig. 5c, right). At TS1, 2HB increases to 45% while 3HB decreases to 11%, coinciding with pronounced dipolar reorientation. The 2HB population remains dominant at Int ($\sim$40%), whereas 0HB decreases to 6%, contrasting sharply with CCM. At TS2, 2HB and 3HB contribute $\sim$40% and $\sim$20%, respectively, reaching 33% each at FS, while 0HB remains near 6%. These results reveal that CPM preserves a greater proportion of multiply hydrogen-bonded water throughout the later reaction stages, suggesting that pronounced dipolar reorientation can occur without the transient loss of HB connectivity observed under CCM.

The contrast is most pronounced at Int, where approximately 30% of water molecules are non-hydrogen-bonded under CCM, compared with only 6% under CPM. By FS, the combined 2HB and 3HB populations account for approximately 66% under CPM, compared with approximately 33% under CCM. This difference reveals that the electrochemical boundary condition influences not only water orientation but also the distribution of local HB coordination during bond formation and cleavage. Notably, the greater HB coordination under CPM does not necessarily imply stronger individual hydrogen bonds or a more rigid network; rather, it reflects a distinct organization of the interfacial hydration environment.

Together, the dipolar and HB analyses reveal that O–O bond formation is accompanied

by continuous reorganization of the interfacial hydration environment, involving both water reorientation and redistribution of HB connectivity, irrespective of the electrochemical description. However, the distinct evolution of these solvent degrees of freedom under CCM and CPM highlights the important role of electrode potential in governing the interfacial response along the reaction coordinate. This coupled evolution of the reactive geometry, electronic environment and solvent structure raises the question of how electron–nuclear interactions respond during O–O bond formation and subsequent Nb–O bond cleavage. We therefore examine the evolution of nonadiabatic coupling (NAC) along the reaction coordinate to characterize the potential-dependent electronic response accompanying these transformations.

Potential-dependent electronic response and nonadiabatic coupling during O–O bond formation

To characterize the electronic response accompanying O–O coupling, we examined the electronic band structure and nonadiabatic coupling (NAC) at the Nb_2Se_2C/water interface under CCM and CPM (Fig. 6). The band structures of the surface-bound *O*O intermediate exhibit dispersive bands crossing the Fermi level (E_F) under both conditions, confirming the metallic character of the interface (Fig. 6a). Despite the substantial difference in O-O coupling barriers between CCM and CPM, the overall band dispersions and distribution of electronic states near E_F remain comparable. This suggests that the influence of the electrochemical boundary condition is not readily captured by the static electronic structure, motivating an examination of its evolution during bond formation.

We therefore tracked the electronic band energies along the collective variable (CV), spanning approximately -0.3 to -5.0. Representative results at the X point are shown in Fig. 6b, with the corresponding evolution at other k-points provided in Supplementary Figs. S6 and S7. Under both conditions, the electronic states near E_F fluctuate as the adjacent oxo species approach, form an O–O bond and undergo subsequent Nb–O bond re-

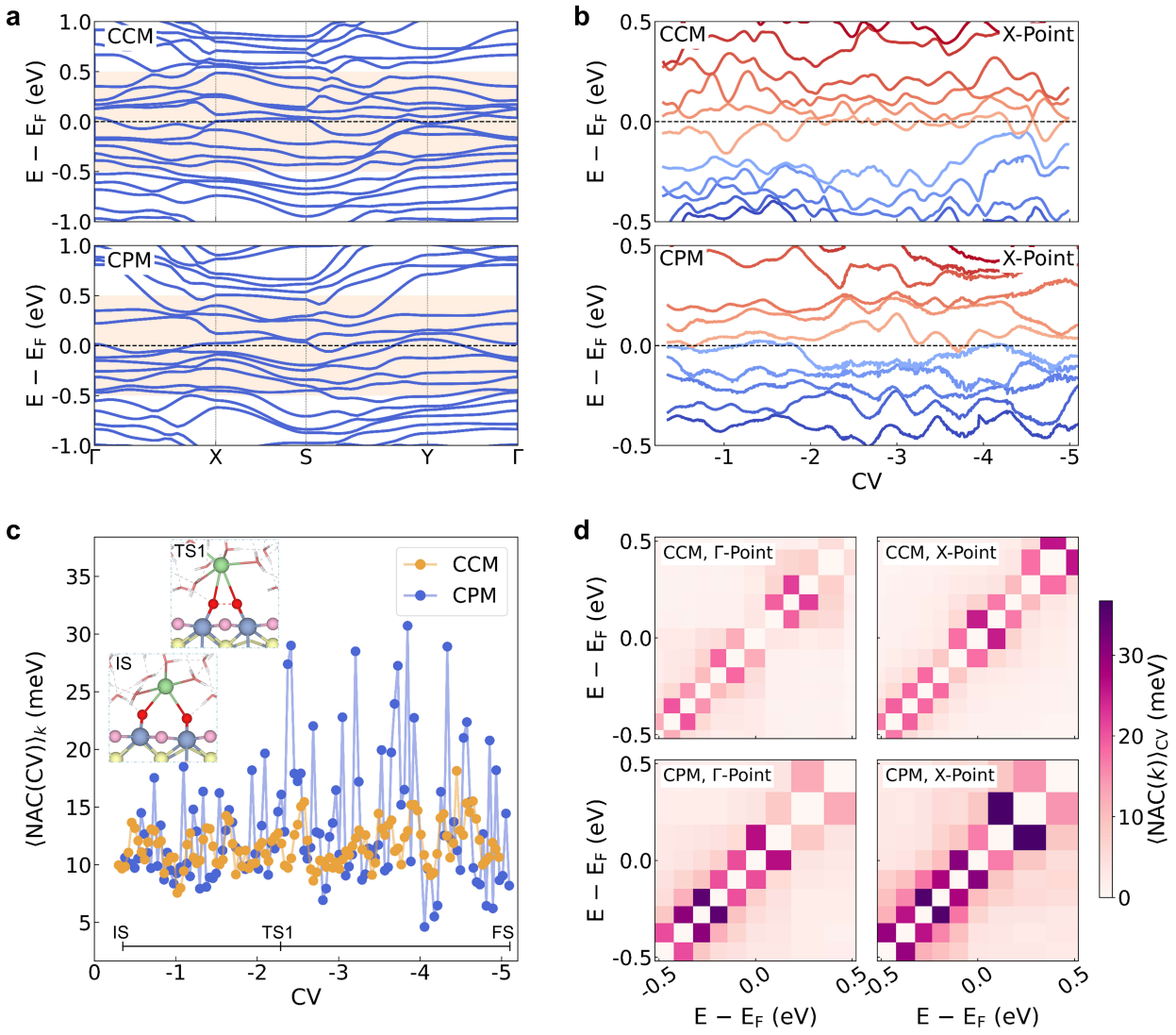

Figure 6: **Electronic structure and nonadiabatic coupling during O–O bond formation. a,** Electronic band structures of the surface-adsorbed *O*O intermediate at the Nb_2Se_2C/water interface, calculated using equilibrium geometries obtained under constant-charge (CCM) and constant-potential (CPM) conditions. **b,** Representative evolution of electronic band energies at the X point along the reaction coordinate (CV), tracking the transformation of adjacent surface oxo species into an O–O dimer, under CCM and CPM. **c,** Evolution of the nonadiabatic coupling (NAC), averaged over k-points, plotted as a function of the CV, under CCM and CPM conditions. **d,** k-point-resolved mean NAC matrices, averaged over configurations sampled across the whole range of CV, under CCM and CPM conditions. Representative results are shown for two high-symmetry k-points, Γ and X.

arrangement. However, CCM exhibits comparatively confined energy fluctuations, whereas CPM produces a broader distribution of instantaneous band energies and more frequent near-approaches between neighbouring electronic states, particularly towards more negative

CV values. These transient reductions in energy separation identify configurations where electronic-state mixing may become more significant, depending on the strength of the associated electron–nuclear coupling.

To quantify this response, we evaluated the k-averaged NAC, $\langle \mathrm{NAC(CV)} \rangle_k$, along the reaction coordinate (Fig. 6c). Under CCM, the coupling remains relatively weak, typically $\sim$10–15 meV, with modest fluctuations. In contrast, CPM exhibits pronounced variations, with transient maxima approaching 30 meV, approximately two to three times the typical CCM values. Although the NAC magnitudes are comparable near the initial state, their divergence becomes evident around TS1 and persists through the subsequent reaction stages (CV ≈ -2.29 to -5), with prominent maxima near CV ≈ -4. The enhanced coupling therefore emerges predominantly during the formation of the bridging Nb1–O1–O2–Nb2 intermediate and subsequent Nb2–O2 bond elongation and cleavage (Fig. 4), indicating that the electronic-state response is sensitive to the evolving bonding environment. Nevertheless, NAC magnitudes alone do not establish the probabilities of nonadiabatic transitions.

To resolve the reciprocal-space dependence of this response, we examined the k-resolved NAC matrices, $\langle \mathrm{NAC}(k) \rangle_{\mathrm{CV}}$, averaged over configurations sampled along the reaction coordinate (Supplementary Figs. S8 and S9). Representative matrices at the Γ and X points reveal comparatively weak coupling under CCM, with the dominant contributions concentrated near the matrix diagonal and limited off-diagonal intensity (Fig. 6d). Under CPM, appreciable off-diagonal contributions extend across a broader range of electronic-state pairs. At Γ, the enhancement is particularly evident among states below E_F, whereas the X point exhibits the strongest overall coupling, including contributions involving states on both sides of E_F. The pronounced response at X is consistent with the frequent near-approaches of electronic levels observed along the CV (Fig. 6b). These results reveal a distinct k-dependence of electron–nuclear coupling, despite the broadly similar static band structures under CCM and CPM.

Overall, these analyses establish that O–O bond formation involves a dynamic electronic

response that depends strongly on the electrochemical boundary condition. Although both descriptions preserve the metallic electronic structure, CPM is associated with larger electronic energy fluctuations, enhanced NAC and a broader distribution of coupled electronic-state pairs during bond formation and cleavage. Alongside the potential-dependent reaction energetics (Fig. 4) and interfacial water reorganization (Fig. 5), these findings reveal that electrode charge regulation is accompanied by changes in both solvent and electronic degrees of freedom along the reaction coordinate. While the enhanced NAC does not establish a direct contribution of nonadiabatic transitions to the reduced activation barrier, it identifies an additional aspect of the interfacial response that is not apparent from static electronic-structure analysis. Thus, a molecular-level description of electrochemical O–O coupling must account for the interplay between electrode potential, evolving bond geometry, solvent reorganization and electronic-state coupling.

Nonlocal charge redistribution and lattice response during O–O coupling

The enhanced NAC under CPM reveals a stronger dynamical interaction between electronic and nuclear degrees of freedom during O–O bond formation. However, the NAC analysis does not establish how the accompanying electronic redistribution is spatially accommodated within the electrode. To address this, we examined the evolution of atomic Bader charges and the structural response of the surrounding lattice along the reaction coordinate (Fig. 7). Particular attention was given to distinguishing the contributions of the primary reaction center, comprising O1, O2, Nb1, Nb2, and K (atoms directly bonded to reactive oxygen species) from those of the neighboring Se and C atoms.

The Bader charge evolution reveals a systematic redistribution of electronic density as the two surface-bound oxygen species approach and form an O–O bond (Fig. 7a). Under both CCM and CPM, the charges of O1 and O2 become progressively less negative toward the final state, indicating a reduction in their assigned electron populations and establishing the

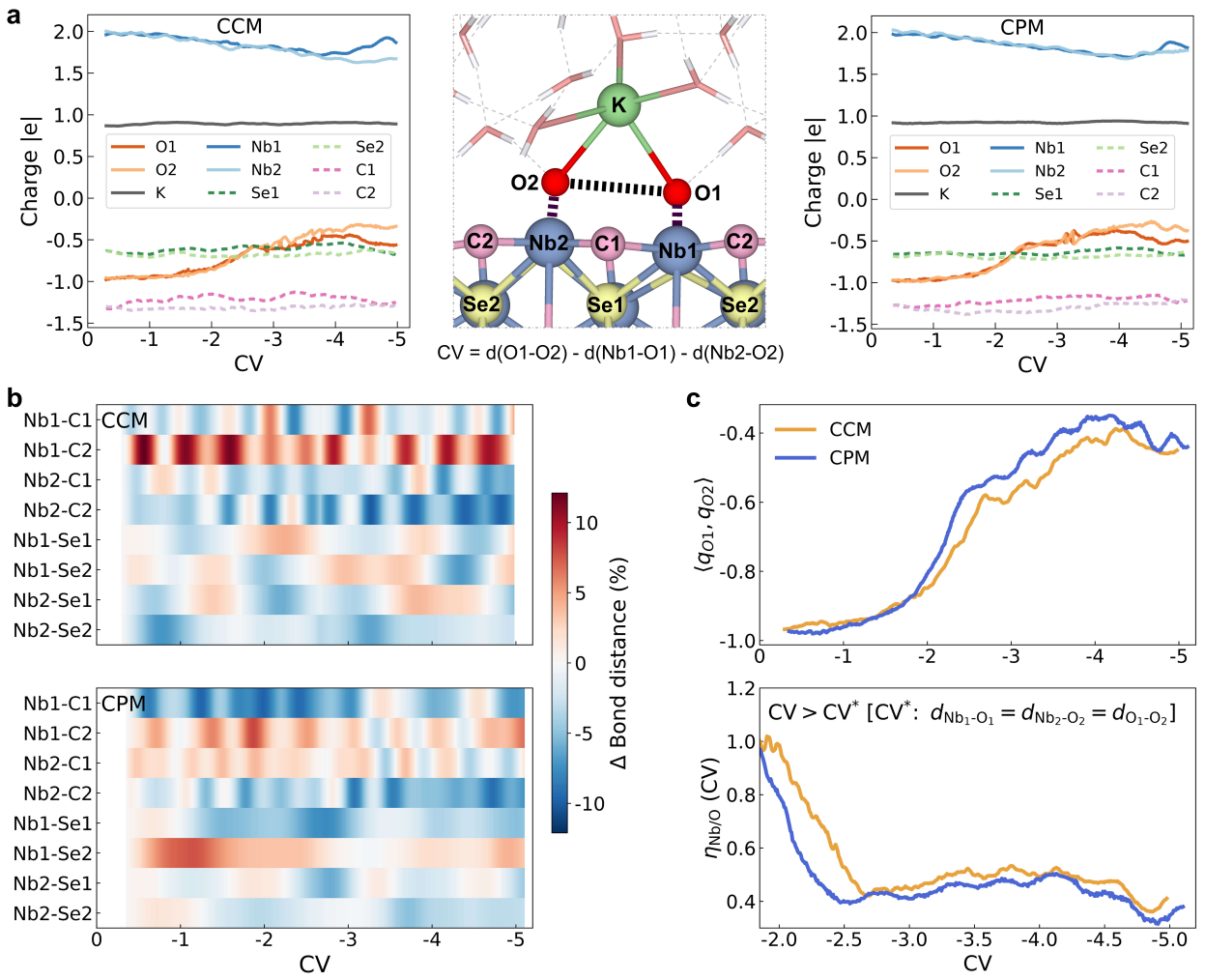

Figure 7: **Charge redistribution and structural response during O–O bond formation. a,** Evolution of Bader charges ($|e|$) on O1, O2, K, Nb1, Nb2, Se1, Se2, C1 and C2 along the collective variable (CV) under constant-charge (CCM, left) and constant-potential (CPM, right) conditions. Solid lines represent primary reaction-site atoms (O1, O2, K, Nb1 and Nb2), whereas dashed lines denote secondary framework atoms (Se1, Se2, C1 and C2). The central structural snapshot identifies the atoms and relevant geometric parameters. **b,** Relative changes in Nb–C and Nb–Se bond lengths (Δ Bond distance, %) along the CV under CCM (top) and CPM (bottom). Red and blue indicate bond elongation and contraction, respectively, relative to the initial configuration. **c,** Evolution of the mean Bader charge of the reactive oxygen atoms, $\langle q_O \rangle = (q_{O1} + q_{O2})/2$ (top), and the local charge-compensation ratio, $\eta_{Nb/O}(CV) = -\Delta q_{Nb}(CV)/\Delta q_O(CV)$ (bottom), under CCM and CPM. Here, Δq_{Nb} and Δq_O denote changes in the combined Bader charges of Nb1/Nb2 and O1/O2, respectively, relative to the reference configuration. The ratio quantifies the extent to which charge redistribution on the directly coordinated Nb atoms compensates changes in the charge of the reactive oxygen pair. It is evaluated beyond CV*, defined by $d_{Nb1-O1} = d_{Nb2-O2} = d_{O1-O2}$.

oxidative character of the coupling process. In contrast, the adjacent Nb1 and Nb2 centers exhibit a decrease in their Bader charges, consistent with partial accumulation of electron density. This opposing evolution indicates that oxidation of the reactive oxygen species is accompanied by electronic redistribution toward the neighboring metal centers. However, the changes are not restricted to the O–O and Nb–O units. Smaller variations are also observed in the Bader charges of the surrounding Se and C atoms, suggesting that the electronic redistribution extends beyond the immediate reaction centre. In contrast, the Bader charge of the interfacial K^+ remains nearly invariant along the CV, suggesting that it primarily provides electrostatic stabilization rather than directly participating in the redox process, despite its proximity to the reactive oxygen species. Although both CCM and CPM exhibit qualitatively similar charge-redistribution trends, differences in their relative magnitudes reveal the sensitivity of the nonlocal electronic response to the imposed electrochemical boundary condition.

The redistribution of electronic density is accompanied by a structural response of the surrounding lattice (Fig. 7b). The relative changes in Nb–C and Nb–Se bond distances reveal simultaneous elongation and contraction of different bonds as the reaction progresses. These changes indicate that the coordination environment surrounding the reactive Nb centers continuously adjusts to the formation of the O–O bond and subsequent asymmetric Nb–O dissociation. Notably, the magnitude and heterogeneity of these bond-length variations are more pronounced under CPM than under CCM, suggesting a stronger structural response of the supporting lattice under constant-potential conditions. Thus, the reaction-induced rearrangement is not confined to the Nb–O bonds directly involved in the coupling event but extends into the neighboring Nb–C and Nb–Se framework. The concurrent evolution of atomic charges and bond distances indicates that electronic redistribution and lattice deformation are coupled during the reaction, consistent with the enhanced electron–nuclear coupling identified from the NAC analysis.

The electronic response of the reacting oxygen atoms is shown in Fig.7c, which tracks

the average Bader charge of O1 and O2, $\langle q_{O1}, q_{O2} \rangle$, along the CV. In both systems, the oxygen atoms start from a charge of about -0.97$|e|$, characteristic of oxide-like oxygen, and become progressively less negative as the O–O distance shortens, reaching about -0.4 $|e|$ at CV ≈ -4 This depletion of electron density indicates that O–O association is accompanied by oxidation-like behavior of the reacting oxygens, with a gradual rather than abrupt redistribution of charge. The increase is steepest between CV -2 and -3 and occurs slightly earlier in CPM than in CCM, suggesting that the onset of O–O bonding is reached earlier along the reaction coordinate under constant-potential conditions. Beyond CV ≈ -4, the charge saturates in both systems.

To quantify the extent to which the electronic redistribution is localized around the reactive Nb centers, we compared the change in the combined Bader charges of Nb1 and Nb2 with that of the two reacting oxygen atoms (Fig. 7c). The charge response was evaluated beyond the characteristic configuration CV*, where $d_{\mathrm{O1-O2}} = d_{\mathrm{Nb1-O1}} = d_{\mathrm{Nb2-O2}}$, marking the onset of substantial O–O association. Defining Δq_{O} and Δq_{Nb} as the changes in the combined Bader charges of the respective atomic pairs relative to initial configuration, the relative charge-compensation contribution can be expressed as

$$\eta_{\mathrm{Nb/O}}(\mathrm{CV}) = -\frac{\Delta q_{\mathrm{Nb}}(\mathrm{CV})}{\Delta q_{\mathrm{O}}(\mathrm{CV})}, \tag{4}$$

where the negative sign accounts for the opposite directions of the oxygen and niobium charge changes. A value of $\eta_{\mathrm{Nb/O}} = 1$ would indicate complete compensation of the oxygen charge change by the two neighboring Nb atoms within this Bader partitioning, whereas deviations from unity indicate that the charge redistribution is not balanced exclusively within these four atoms.

The resulting charge-compensation profiles reveal that the electron-density changes associated with O–O coupling are not confined to the immediate O–Nb coordination environment (Fig. 7c). Although the oxygen atoms progressively lose electron density and the neighboring Nb centers gain electron density, their charge variations do not compensate on a one-to-one

basis. The persistent deviation of $\eta_{\mathrm{Nb/O}}$ from unity indicates that additional regions of the system participate in accommodating the evolving charge distribution. This observation is consistent with the simultaneous, albeit smaller, Bader charge variations of the surrounding Se and C atoms and the accompanying changes in the Nb–C and Nb–Se bond distances. Together, these results establish that the electronic response to O–O coupling extends beyond the primary reaction center and involves the surrounding electrode framework.

The distinction between CCM and CPM becomes particularly evident in the relative charge-compensation response. Under CCM, a larger fraction of the oxygen charge variation is accompanied by an opposing change at the neighboring Nb centers, indicating a comparatively greater contribution from the immediate metal–oxygen coordination environment. Under CPM, the smaller Nb-to-O charge-compensation ratio suggests that a reduced fraction of the oxygen charge change is accommodated locally by Nb1 and Nb2. Instead, the remaining redistribution must involve other electronic degrees of freedom within the modeled interface, including the surrounding electrode framework and, potentially, the external electron reservoir. This difference is consistent with the fundamental distinction between the two electrochemical descriptions: CCM constrains the total electron number, whereas CPM permits electron exchange with a reservoir to maintain the prescribed electrode potential. Consequently, the electronic response under CPM is not restricted to redistribution within a fixed-electron-number system, allowing the electrode charge to adjust as the local bonding environment evolves.

The combined charge and structural analyses therefore provide a spatial perspective on the dynamical electronic response identified from the NAC calculations. The stronger and more broadly distributed NAC under CPM indicates enhanced coupling between electronic states during nuclear rearrangement, while the Bader charge analysis reveals that the accompanying electronic redistribution is not limited to the reactive oxygen atoms and their nearest Nb neighbors. The larger Nb–C and Nb–Se bond distortions under CPM further suggest that the surrounding lattice participates in accommodating these changes. Although

NAC and Bader charges characterize different aspects of the electronic response, their correlated evolution supports a picture in which O–O coupling involves collective adjustments of the electronic structure and local coordination environment rather than an isolated electron-transfer event between two oxygen atoms and their adjacent metal centers.

These findings extend the mechanistic interpretation of the pronounced potential dependence of direct O–O coupling. Under CCM, the reaction proceeds within a fixed-electron-number environment, with a comparatively larger contribution from local Nb–O charge compensation and a more limited dynamical electronic response. Under CPM, the ability to regulate the electrode charge is accompanied by enhanced electron–nuclear coupling, broader charge redistribution, and a more pronounced structural response of the surrounding lattice. Together with the previously identified reorganization of interfacial water, these observations suggest that the lower activation barrier under CPM is associated with the collective response of the electrode–electrolyte interface. The reaction therefore cannot be described solely in terms of local O–O bond formation and Nb–O bond cleavage; it also involves nonlocal electronic redistribution and structural relaxation extending into the supporting electrode framework. This interplay between local bond rearrangement, nonlocal charge accommodation, and interfacial solvent dynamics highlights the importance of treating the electrode potential explicitly when describing the microscopic mechanisms of electrochemical O–O coupling.

Conclusion

Our findings reveal how electrode potential governs direct O–O bond formation through coupled electronic, structural and solvent dynamics at the electrochemical interface. Using Nb_2Se_2C as a model catalyst, we demonstrate that constant-potential conditions promote the sequential oxidation of surface-bound water into adjacent oxo species, accompanied by proton redistribution through the interfacial HB network. The combined effects of electrode

charge regulation and interfacial K^+ lower the predicted oxygen evolution overpotential from 1.00 to 0.31 V. More strikingly, constant-potential conditions reduce the calculated kinetic barrier for direct O–O coupling from 3.43 to 0.49 eV, revealing a pronounced sensitivity of the bond-formation pathway to the electrochemical boundary condition.

This potential dependence extends beyond the immediate reaction center. O–O bond formation is accompanied by substantial reorganization of interfacial water, enhanced nonadiabatic electronic coupling and charge redistribution involving both the reactive Nb–O units and the surrounding electrode framework. These correlated responses reveal that electrochemical O–O coupling cannot be adequately understood as an isolated bond-forming event, but involves collective adjustments of the electrode–electrolyte interface. These results provide transferable mechanistic insights into alternative OER pathways and guiding the understanding of oxygen evolution at electrified catalytic interfaces. More broadly, our findings reveal that electrode charge regulation involves nonlocal electronic redistribution and nonadiabatic electron–nuclear coupling, providing a molecular-level framework for understanding catalytic bond formation at electrified interfaces. Electrode potential thus governs not only reaction thermodynamics but also the kinetic pathways through which interfacial electronic and nuclear degrees of freedom evolve.

Computational Details

Electronic structure and electrochemical interface

Spin-polarized density functional theory (DFT) calculations were performed using the Vienna *Ab initio* Simulation Package (VASP),[54] employing the projector-augmented-wave method.[55] The exchange–correlation and dispersion treatments were benchmarked against the structural properties of Nb_2Se_2C, as detailed in the Supplementary Methods. To capture the dynamic response of the electrified Nb_2Se_2C/water interface, we employed a constant-potential hybrid-solvation dynamics model (CP-HS-DM), implemented in CP-VASP.[51,52] The frame-

work combines explicit interfacial water with continuum solvation[56] and couples the electronic system to a fictitious potentiostat,[57] allowing the electron population to evolve dynamically while maintaining a prescribed electrode potential. This grand-canonical treatment enables the interfacial charge distribution and solvent environment to respond self-consistently to chemical transformations, in contrast to conventional fixed-electron-number simulations. Thus, two electrochemical boundary conditions were applied: the constant charge method (CCM), in which the total number of electrons is fixed and the electrode potential evolves as the reaction proceeds, and the constant potential method (CPM), in which the electrode potential is held fixed and the number of electrons fluctuates through exchange with an electron reservoir. In the CPM simulations, the electrode potential was set to 0V with respect to the standard hydrogen electrode (SHE), obtained by referencing the computed Fermi level to the absolute SHE potential of 4.6 V.**??**

Reaction dynamics and electronic coupling

First-principles molecular dynamics simulations were performed in the canonical (NVT) ensemble at 300 K using a Nosé–Hoover thermostat and a time step of 1 fs. To resolve the influence of electrochemical boundary conditions on O–O bond formation, we combined constrained *ab initio* molecular dynamics (AIMD) with slow-growth enhanced sampling[53] under constant-charge (CCM) and constant-potential (CPM) conditions. In the latter, the electronic population was updated every five molecular dynamics steps to maintain the prescribed electrode potential, allowing the electronic response to evolve concurrently with structural rearrangements.

The direct O–O coupling pathway was described using a collective variable (ε) that simultaneously captures O–O bond formation and the weakening of the two surface Nb–O bonds:

$$\varepsilon = d_{\mathrm{O_1-O_2}} - d_{\mathrm{Nb_1-O_1}} - d_{\mathrm{Nb_2-O_2}}, \tag{5}$$

where $d_{\mathrm{O_1-O_2}}$ represents the forming O–O bond, whereas $d_{\mathrm{Nb_1-O_1}}$ and $d_{\mathrm{Nb_2-O_2}}$ describe the evolving metal–oxygen coordination. Notably, ε is referred to as the collective variable (CV) throughout the manuscript. The reaction coordinate was progressively advanced at a rate of -2×10^{-3} Å fs^{-1}, enabling continuous sampling of the coupled bond-formation and bond-cleavage processes.

The reaction energetics were evaluated by integrating the generalized force along the reaction coordinate. In the reversible thermodynamic-integration limit, the free-energy change was expressed as

$$\Delta W = \int_{\varepsilon_{\mathrm{IS}}}^{\varepsilon_{\mathrm{FS}}} \left\langle \frac{\partial H}{\partial \varepsilon} \right\rangle_{\varepsilon} d\varepsilon, \tag{6}$$

where H is the system Hamiltonian and the brackets denote constrained ensemble averaging. The corresponding mean-force evaluation follows the Blue-Moon ensemble formalism,[58] with geometric constraints enforced through the SHAKE algorithm.[59] The relation between finite-rate slow-growth work and equilibrium free energies, together with the detailed sampling procedure, is provided in the Supplementary Methods.[60]

To examine the electronic response accompanying the structural transformations, nonadiabatic coupling (NAC) matrix elements were evaluated along the constrained AIMD trajectories using CA-NAC,[61] which employs the concentric approximation within the projector-augmented-wave formalism. The coupling between electronic states j and k induced by nuclear motion is defined as

$$D_{jk}(t) = \langle \phi_j \left| \nabla_{\mathbf{R}} \right| \phi_k \rangle \cdot \dot{\mathbf{R}} = \left\langle \phi_j \left| \frac{\partial}{\partial t} \right| \phi_k \right\rangle, \tag{7}$$

where ϕ_j and ϕ_k are the electronic wavefunctions and $\dot{\mathbf{R}}$ denotes the nuclear velocity. The coupling was evaluated using the symmetric finite-difference formulation of Hammes-Schiffer and Tully,[62]

$$D_{jk}(t) \approx \frac{1}{2\Delta t}\left[\langle \phi_j(t)|\phi_k(t+\Delta t)\rangle - \langle \phi_j(t+\Delta t)|\phi_k(t)\rangle\right]. \tag{8}$$

NAC matrix elements were evaluated for pairs of Kohn–Sham states within $E_F \pm 0.5$ eV at each sampled **k**-point and subsequently averaged over the Brillouin zone.

Notes

The authors declare no competing financial interest.

Supporting Information Available

1. Figure S1: Validation of the computational method against experiment
2. Figure S2: Sensitivity of the interfacial water-density profile to the spatial averaging window.
3. Figure S3: Comparison of the AEM and OPM intermediates at the Nb_2Se_2C/water interface in the presence of solvated K^+.
4. Figures S4 and S5: Sensitivity of the hydrogen-bond statistics to the H—O distance cutoff under CCM and CPM respectively.
5. Figures S6 and S7: Evolution of the band energies for all high-symmetry k-points as a function of the collective variable (CV) under CCM and CPM respectively during O-O coupling process.
6. Figures S8 and S9: The k-point-resolved NAC matrices, averaged over collective-variable configurations sampled along the reaction coordinate under CCM and CPM condition respectively.

Acknowledgement

S.B. gratefully acknowledges support from SERB, DST, India for the Core Research Grant (CRG/2022/009476) and CSIR for EMR-II/ASPIRE research grant. R.S. acknowledges the University Grants Commission (UGC), New Delhi for the Senior research fellowship. All authors acknowledge the National Supercomputing Mission (NSM), C-DAC, and Ministry of Electronics and Information Technology (MeitY) for the High-performance computing (PARAM Ganga) facility at IIT Roorkee.

Data availability

The datasets generated and/or analyzed in this study are available in the Source Data at https://github.com/CLEANdatahub/Potential-Dependent-Oxygen-Evolution-.git

Code availability

The relevant scripts, structures, and details are available at Source Code https://github.com/CLEANdatahub/Potential-Dependent-Oxygen-Evolution-.git

References

(1) Stamenkovic, V. R.; Strmcnik, D.; Lopes, P. P.; Markovic, N. M. Energy and fuels from electrochemical interfaces. *Nature materials* **2017**, *16*, 57–69.

(2) Roger, I.; Shipman, M. A.; Symes, M. D. Earth-abundant catalysts for electrochemical and photoelectrochemical water splitting. *Nature Reviews Chemistry* **2017**, *1*, 0003.

(3) Fabbri, E.; Schmidt, T. J. Oxygen evolution reaction—the enigma in water electrolysis. *Acs Catalysis* **2018**, *8*, 9765–9774.

(4) Quan, L.; Jiang, H.; Mei, G.; Sun, Y.; You, B. Bifunctional electrocatalysts for overall and hybrid water splitting. *Chemical Reviews* **2024**, *124*, 3694–3812.

(5) Xie, X.; Du, L.; Yan, L.; Park, S.; Qiu, Y.; Sokolowski, J.; Wang, W.; Shao, Y. Oxygen evolution reaction in alkaline environment: material challenges and solutions. *Advanced Functional Materials* **2022**, *32*, 2110036.

(6) Spöri, C.; Kwan, J. T. H.; Bonakdarpour, A.; Wilkinson, D. P.; Strasser, P. The stability challenges of oxygen evolving catalysts: towards a common fundamental understanding and mitigation of catalyst degradation. *Angewandte Chemie International Edition* **2017**, *56*, 5994–6021.

(7) Adamji, H.; Kevlishvili, I.; Kastner, D. W.; Meyer, R.; Román-Leshkov, Y.; Kulik, H. J. Multiobjective Optimization of Synthetically Accessible Homogeneous Catalysts Reveals Tradeoffs for Methane-to-Methanol Conversion. *ACS Catalysis* **2026**, *16*, 21057–21076.

(8) Seh, Z. W.; Kibsgaard, J.; Dickens, C. F.; Chorkendorff, I.; Nørskov, J. K.; Jaramillo, T. F. Combining theory and experiment in electrocatalysis: Insights into materials design. *Science* **2017**, *355*, eaad4998.

(9) Jones, T. E.; Teschner, D.; Piccinin, S. Toward realistic models of the electrocatalytic oxygen evolution reaction. *Chemical reviews* **2024**, *124*, 9136–9223.

(10) Rossmeisl, J.; Logadottir, A.; Nørskov, J. K. Electrolysis of water on (oxidized) metal surfaces. *Chemical physics* **2005**, *319*, 178–184.

(11) Rossmeisl, J.; Qu, Z.-W.; Zhu, H.; Kroes, G.-J.; Nørskov, J. K. Electrolysis of water on oxide surfaces. *Journal of Electroanalytical Chemistry* **2007**, *607*, 83–89.

(12) Koper, M. T. Theory of multiple proton–electron transfer reactions and its implications for electrocatalysis. *Chemical science* **2013**, *4*, 2710–2723.

(13) Song, J.; Wei, C.; Huang, Z.-F.; Liu, C.; Zeng, L.; Wang, X.; Xu, Z. J. A review on fundamentals for designing oxygen evolution electrocatalysts. *Chemical Society Reviews* **2020**, *49*, 2196–2214.

(14) Craig, M. J.; Coulter, G.; Dolan, E.; Soriano-López, J.; Mates-Torres, E.; Schmitt, W.; García-Melchor, M. Universal scaling relations for the rational design of molecular water oxidation catalysts with near-zero overpotential. *Nature communications* **2019**, *10*, 4993.

(15) Rong, X.; Parolin, J.; Kolpak, A. M. A fundamental relationship between reaction mechanism and stability in metal oxide catalysts for oxygen evolution. *ACS catalysis* **2016**, *6*, 1153–1158.

(16) Zagalskaya, A.; Alexandrov, V. Role of defects in the interplay between adsorbate evolving and lattice oxygen mechanisms of the oxygen evolution reaction in RuO2 and IrO2. *ACS Catalysis* **2020**, *10*, 3650–3657.

(17) Zhang, L.; Wang, L.; Wen, Y.; Ni, F.; Zhang, B.; Peng, H. Boosting neutral water oxidation through surface oxygen modulation. *Advanced Materials* **2020**, *32*, 2002297.

(18) Geiger, S.; Kasian, O.; Ledendecker, M.; Pizzutilo, E.; Mingers, A. M.; Fu, W. T.; Diaz-Morales, O.; Li, Z.; Oellers, T.; Fruchter, L.; others The stability number as a metric for electrocatalyst stability benchmarking. *Nature Catalysis* **2018**, *1*, 508–515.

(19) Wen, Y.; Chen, P.; Wang, L.; Li, S.; Wang, Z.; Abed, J.; Mao, X.; Min, Y.; Dinh, C. T.; Luna, P. D.; others Stabilizing highly active Ru sites by suppressing lattice oxygen participation in acidic water oxidation. *Journal of the American Chemical Society* **2021**, *143*, 6482–6490.

(20) Zheng, X.; Jiang, L.; Pan, H.; Sun, W. Breaking the activity-durability trade-off of anode catalysts for proton exchange membrane water electrolyzers. *ACS Energy Letters* **2025**, *10*, 3471–3484.

(21) Rong, C.; Huang, X.; Arandiyan, H.; Shao, Z.; Wang, Y.; Chen, Y. Advances in oxygen evolution reaction electrocatalysts via direct oxygen–oxygen radical coupling pathway. *Advanced Materials* **2025**, *37*, 2416362.

(22) Zhu, W.; Yao, F.; Cheng, K.; Zhao, M.; Yang, C.-J.; Dong, C.-L.; Hong, Q.; Jiang, Q.; Wang, Z.; Liang, H. Direct dioxygen radical coupling driven by octahedral ruthenium–oxygen–cobalt collaborative coordination for acidic oxygen evolution reaction. *Journal of the American Chemical Society* **2023**, *145*, 17995–18006.

(23) Wang, N.; Ou, P.; Miao, R. K.; Chang, Y.; Wang, Z.; Hung, S.-F.; Abed, J.; Ozden, A.; Chen, H.-Y.; Wu, H.-L.; others Doping shortens the metal/metal distance and promotes OH coverage in non-noble acidic oxygen evolution reaction catalysts. *Journal of the American Chemical Society* **2023**, *145*, 7829–7836.

(24) Liang, J.; Gao, X.; Xu, K.; Lu, J.; Liu, D.; Zhao, Z.; Tse, E. C.; Peng, Z.; Zhang, W.; Liu, J. Unraveling the asymmetric O O radical coupling mechanism on Ru O Co for enhanced acidic water oxidation. *Small* **2023**, *19*, 2304889.

(25) Lin, C.; Li, J.-L.; Li, X.; Yang, S.; Luo, W.; Zhang, Y.; Kim, S.-H.; Kim, D.-H.; Shinde, S. S.; Li, Y.-F.; others In-situ reconstructed Ru atom array on α-MnO2 with enhanced performance for acidic water oxidation. *Nature catalysis* **2021**, *4*, 1012–1023.

(26) Gauthier, J. A.; Dickens, C. F.; Chen, L. D.; Doyle, A. D.; Nørskov, J. K. Solvation effects for oxygen evolution reaction catalysis on IrO2 (110). *The Journal of Physical Chemistry C* **2017**, *121*, 11455–11463.

(27) Wang, Z.; Goddard III, W. A.; Xiao, H. Potential-dependent transition of reaction mechanisms for oxygen evolution on layered double hydroxides. *Nature Communications* **2023**, *14*, 4228.

(28) Zhu, S.; Yang, R.; Li, H. J. W.; Huang, S.; Wang, H.; Liu, Y.; Li, H.; Zhai, T. Re-

constructing hydrogen-bond network for efficient acidic oxygen evolution. *Angewandte Chemie International Edition* **2024**, *63*, e202319462.

(29) Lounasvuori, M.; Mathis, T. S.; Gogotsi, Y.; Petit, T. Hydrogen-bond restructuring of water-in-salt electrolyte confined in Ti3C2Tx MXene monitored by operando infrared spectroscopy. *The journal of physical chemistry letters* **2023**, *14*, 1578.

(30) He, X.; Iliescu, A.; Yang, T.; Arguilla, M. Q.; Chen, T.; Kulik, H. J.; Dinca, M. Reversible O–O Bond Scission and O2 Evolution at MOF-Supported Tetramanganese Clusters. *Journal of the American Chemical Society* **2023**, *145*, 16872–16878.

(31) Guha, A.; Seemakurthi, R. R.; Polesso, B.; Haldar, P.; Ram, R.; Pinilla-Sánchez, A.; Mondal, I.; Kernan, D.; López, N.; García de Arquer, F. P. Operando resolution of CO2 electrolysis interfaces at application-relevant current density reveals water gating. *Nature Catalysis* **2026**, 1–14.

(32) Nørskov, J. K.; Rossmeisl, J.; Logadottir, A.; Lindqvist, L.; Kitchin, J. R.; Bligaard, T.; Jonsson, H. Origin of the overpotential for oxygen reduction at a fuel-cell cathode. *The Journal of Physical Chemistry B* **2004**, *108*, 17886–17892.

(33) Chen, Z.; Chen, L.; Wen, Z.; Jiang, Q. Understanding electro-catalysis by using density functional theory. *Physical Chemistry Chemical Physics* **2019**, *21*, 23782–23802.

(34) Exner, K. S. Is thermodynamics a good descriptor for the activity? Re-investigation of Sabatier's principle by the free energy diagram in electrocatalysis. *ACS Catalysis* **2019**, *9*, 5320–5329.

(35) Chen, B. W.; Xu, L.; Mavrikakis, M. Computational methods in heterogeneous catalysis. *Chemical Reviews* **2021**, *121*, 1007–1048.

(36) Wilson, J. C.; Caratzoulas, S.; Vlachos, D. G.; Yan, Y. Insights into solvent and surface

charge effects on Volmer step kinetics on Pt (111). *Nature Communications* **2023**, *14*, 2384.

(37) Sundararaman, R.; Goddard, W. A.; Arias, T. A. Grand canonical electronic density-functional theory: Algorithms and applications to electrochemistry. *The Journal of chemical physics* **2017**, *146*.

(38) Kim, D.; Shi, J.; Liu, Y. Substantial impact of charge on electrochemical reactions of two-dimensional materials. *Journal of the American Chemical Society* **2018**, *140*, 9127–9131.

(39) Liu, Z.; Sun, Y.-F.; Wang, Y.-S.; Zhang, W.; Gan, L.-H.; Liu, X.-H.; Zhao, L.-B. Optimal solution for modeling electrocatalysis on two-dimensional single-atom catalysts with grand canonical DFT. *ACS Catalysis* **2025**, *15*, 7993–8004.

(40) Majed, A.; Kothakonda, M.; Wang, F.; Tseng, E. N.; Prenger, K.; Zhang, X.; Persson, P. O.; Wei, J.; Sun, J.; Naguib, M. Transition metal carbo-chalcogenide "TMCC:" a new family of 2D materials. *Advanced Materials* **2022**, *34*, 2200574.

(41) Hu, T.; Wang, M.; Cai, C.; Cheng, R.; Wang, J.; Guo, C.; Ren, L.; Li, C. M.; Wang, X. Van der Waals Transition Metal Carbo-Chalcogenides: Theoretical Screening and Charge Storage. *Small* **2024**, *20*, 2402076.

(42) Zhang, Y.; Zhou, Q.; Zhu, J.; Yan, Q.; Dou, S. X.; Sun, W. Nanostructured metal chalcogenides for energy storage and electrocatalysis. *Advanced Functional Materials* **2017**, *27*, 1702317.

(43) Zhu, C. R.; Gao, D.; Ding, J.; Chao, D.; Wang, J. TMD-based highly efficient electrocatalysts developed by combined computational and experimental approaches. *Chemical Society Reviews* **2018**, *47*, 4332–4356.

(44) Fu, Z.; Wang, N.; Legut, D.; Si, C.; Zhang, Q.; Du, S.; Germann, T. C.; Francisco, J. S.; Zhang, R. Rational design of flexible two-dimensional MXenes with multiple functionalities. *Chemical reviews* **2019**, *119*, 11980–12031.

(45) Fan, K.; Zou, H.; Lu, Y.; Chen, H.; Li, F.; Liu, J.; Sun, L.; Tong, L.; Toney, M. F.; Sui, M.; others Direct observation of structural evolution of metal chalcogenide in electrocatalytic water oxidation. *ACS nano* **2018**, *12*, 12369–12379.

(46) Ng, V. M. H.; Huang, H.; Zhou, K.; Lee, P. S.; Que, W.; Xu, J. Z.; Kong, L. B. Recent progress in layered transition metal carbides and/or nitrides (MXenes) and their composites: synthesis and applications. *Journal of Materials Chemistry A* **2017**, *5*, 3039–3068.

(47) Zhang, Y.; Chen, M.; Zhang, T.; Parker, T.; Zhang, D.; Wang, R.; Kim, H.; Michałowski, P. P.; Kornyshev, A.; Gogotsi, Y. Water-Mediated Ion Selectivity in 2D MXene Channels. *Journal of the American Chemical Society* **2026**,

(48) Beckmann, O.; Boller, H.; Nowotny, H. Die kristallstrukturen von ta2s2c und ti4s5 (ti0, 81s). *Monatshefte für Chemie/Chemical Monthly* **1970**, *101*, 945–955.

(49) Boller, H.; Hiebl, K. Quaternary pseudo-intercalation phases Tx [Nb2S2C](T V, Cr, Mn, Fe, Co, Ni, Cu) and metastable Nb2S2C formed by topochemical synthesis. *Journal of alloys and compounds* **1992**, *183*, 438–443.

(50) Pang, X.; Wu, T.; Gu, Y.; Wang, D.; Che, X.; Sun, D.; Huang, F. Nb2Se2C: a new compound as a combination of transition metal dichalcogenide and MXene for oxygen evolution reaction. *Chemical Communications* **2020**, *56*, 9036–9039.

(51) Zhao, X.; Liu, Y. Origin of selective production of hydrogen peroxide by electrochemical oxygen reduction. *Journal of the American Chemical Society* **2021**, *143*, 9423–9428.

(52) Yu, S.; Levell, Z.; Jiang, Z.; Zhao, X.; Liu, Y. What is the rate-limiting step of oxygen reduction reaction on Fe–N–C catalysts? *Journal of the American Chemical Society* **2023**, *145*, 25352–25356.

(53) Woo, T. K.; Margl, P. M.; Blöchl, P. E.; Ziegler, T. A combined Car- Parrinello QM/MM implementation for ab initio molecular dynamics simulations of extended systems: application to transition metal catalysis. *The Journal of Physical Chemistry B* **1997**, *101*, 7877–7880.

(54) Kresse, G.; Furthmüller, J. Efficient iterative schemes for ab initio total-energy calculations using a plane-wave basis set. *Physical review B* **1996**, *54*, 11169.

(55) Blöchl, P. E. Projector augmented-wave method. *Physical review B* **1994**, *50*, 17953.

(56) Mathew, K.; Kolluru, V.; Mula, S.; Steinmann, S. N.; Hennig, R. G. Implicit self-consistent electrolyte model in plane-wave density-functional theory. *The Journal of chemical physics* **2019**, *151*.

(57) Bonnet, N.; Morishita, T.; Sugino, O.; Otani, M. First-principles molecular dynamics at a constant electrode potential. *Physical Review Letters* **2012**, *109*, 266101.

(58) Carter, E. A.; Ciccotti, G.; Hynes, J. T.; Kapral, R. Constrained reaction coordinate dynamics for the simulation of rare events. *Chemical Physics Letters* **1989**, *156*, 472–477.

(59) Ryckaert, J.-P.; Ciccotti, G.; Berendsen, H. J. Numerical integration of the cartesian equations of motion of a system with constraints: molecular dynamics of n-alkanes. *Journal of computational physics* **1977**, *23*, 327–341.

(60) Jarzynski, C. Nonequilibrium equality for free energy differences. *Physical review letters* **1997**, *78*, 2690.

(61) Chu, W.; Prezhdo, O. V. Concentric approximation for fast and accurate numerical evaluation of nonadiabatic coupling with projector augmented-wave pseudopotentials. *The Journal of Physical Chemistry Letters* **2021**, *12*, 3082–3089.

(62) Hammes-Schiffer, S.; Tully, J. C. Proton transfer in solution: Molecular dynamics with quantum transitions. *The Journal of chemical physics* **1994**, *101*, 4657–4667.

Supplementary Files

This is a list of supplementary files associated with this preprint. Click to download.

- SupplementaryInformation.pdf